

Extraction of surface defects using morphological pyramid and watershed: example of ferrite cores

M. NIENIEWSKI

*Institute of Fundamental Technological Research
Świętokrzyska 21, 00-049 Warszawa, Poland
mmieniew@ippt.gov.pl*

*Electrotechnical Institute
Pozaryskiego 28, 04-703 Warszawa, Poland*

The paper describes a vision system for detection and extraction of the masks of defects on the surface of ferrite cores. Separate approaches are used for small and large defects.

The system for small defects uses a morphological defect detector and a morphological pyramid for detecting positions of defects. Optimization of the performance of the morphological pyramid is carried out by means of the genetic algorithm. Information obtained from the pyramid on the position and extent of defects gives a very coarse approximation of the shape of defects. Using this information, the exact shape of the small defects is then obtained by means of two consecutive morphological reconstructions.

The system for large defects uses the information obtained while attempting to detect small defects. In addition to this, however, it uses the watershed segmentation for extracting the exact shape of large defects. In particular, the output from the watershed segmentation is processed by the region classifier which decides upon which regions from the segmentation should be included into a defect and into a defect free area.

The paper also discusses problems related to extraction of cracks of ferrite cores. A fair number of included examples confirm that the described vision system correctly identifies and extracts a large range of defects of ferrite cores.

1. Introduction

The problem of defects in the manufacturing of ferrite cores is quite a serious one [1, 2]. The manufacturing process includes compacting and sintering ceramic powders which possess the required magnetic properties. The raw material is put into special forms, and after sintering, some surfaces of

the cores are ground to required dimensions. Many distortions of the shape and of the dimensions of the cores arise during the manufacturing process, which takes place at temperatures in the range of 1000°C. The unpredictability of the final product may be appreciated by considering the fact that the reduction of the volume of the cores during the manufacturing process is up to 30%. The nature of defects can be quite diversified. Among the most typical defects are: chippings, ragged edges, pull-outs, cracks, scratches, and discolorations. Most of these defects lead to or are indicative of a loss of the required magnetic properties of the cores. This is the reason why it is very important to guarantee that the cores be manufactured without defects, or at least the number of defects should be maintained at a low level. Of course, defect detection has to be carried out with sufficient speed so that the manufacturing process would not be delayed. Apart from the on-line detection of defects, it is often necessary to carry out classification of defects as well. In this case the results of defect extraction are used as an input to the defect classifier. Defect classification is an off-line process, which also cannot be overly time-consuming.

Detection of surface defects has been investigated in numerous papers. In the following a short review is presented of the papers which use methods similar to or competitive to the one described in this paper.

A sound theoretical approach to defect detection is presented in [3], where structural opening and a top-hat transform are used. Unfortunately, the proposed method is suitable mainly to artificially generated textures. In fact, this method is based on "learning the texture", which involves finding the minimal family of structuring elements corresponding to the primitive patterns found in the analyzed texture. However, finding such a family for ferrite cores is impossible since the textures on the walls of ferrites do not exhibit sufficient stationarity in a single image as well as among images of various cores.

In [4] the use of morphological operations for detection of defects on the matte surface of a TV tube is described. The defects considered have a form of long, thin, and twisted shapes, whereas noise reveals itself in a form of rounded circular blobs. The image is binarized, and the skeletons of all the shapes are found. Differentiation between defects and noise is based on the analysis of the skeletons.

Another method of defect detection is presented in [5], where defects are detected by means of improved versions of the top-hat transform. This approach was subsequently developed into a method of decomposition of shapes in variable resolution [6] and used for detecting defects of textiles, wood, and wire mesh. However, examples considered did not come from the production line. Furthermore, the proposed method is inappropriate for ferrite cores.

The ferrite core is usually shown to the camera as a complete object, and not just as a single flat surface. There are various surfaces, edges, supporting elements, shadows, etc. visible in the image. Defects have to be detected on the walls of the core as well as on the edges. An additional difficulty stems from the fact that defects change in a wide range of sizes, shapes, and depths.

The aim of this paper is to present a method developed for inspection of the ferrite cores. It would be overly optimistic to expect that the morphological methods would make it possible to extract and classify all possible kinds of defects appearing in the manufacturing process. Nevertheless it was proved that a large class of the most commonly encountered defects can be detected and extracted, and this is already a step forward in the automation of the manufacturing of ferrite cores because up to now the human operators had to evaluate the cores.

The details of defect classification for ferrite cores are described in the companion paper [7] included in this book. The defect classifier assigns each pixel to a certain class of defects, such as chippings, pull-outs, etc. or to a defect free area. The classifier gives highly reliable results, but its main drawback is a significant time consumption. By using the defect extraction system one restricts the image area that has to be analyzed by the defect classifier and reduces the classification time by at least one order of magnitude.

2. Principle of Detection of Small Defects

Detection of defects is based on finding brightness irregularities [8]. The principle of detecting such spots is based on the equation, which can be viewed as an improved version of the top-hat transformation. The equation valid for the case of a defect brighter than the surroundings has the form

$$T = I - \min [(I \bullet B) \circ B, I], \quad (2.1)$$

in which I is the original image, T is the gray level map of defects, and B is the structuring element, typically of size 3×3 . The symbol \bullet stands for closing, and \circ for opening. Equation (2.1) is a modification of the original equation for the top-hat transform $T = I - I \circ B$. The latter equation does not have any provision for noise removal. A nonzero output T may then result from the occurrence of defects as well as from noise. In contrast, the operations of closing and opening (C-O) in Eq. (2.1) form a morphological filter, hence the output T becomes less noisy. A graphical interpretation of Eq. (2.1) is shown in Fig. 1, in which a heavy line represents the gray level distribution for a 1-D case, and the spike represents a defect. The ball rolling above the heavy line comes to touch with all the points of a heavy line, which

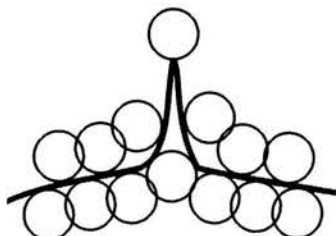


FIGURE 1. Principle of defect detection.

means that the closing does not change the heavy line. The ball rolling below the line obtained from the closing represents the opening. The ball cannot get into the narrow spike, and the points on the circumference of the ball do not reach the heavy line. Hence, the result of the opening lies below the heavy line. The difference indicates that there is a defect.

A typical image of some part of a ferrite core is shown below in Fig. 4(a). The output from the morphological defect detector is a gray level image T , in which all pixels representing defect free areas are painted in black. The pixels belonging to defects are painted with a certain shade of gray which represents the measure of defectiveness at a given pixel. This means that the map of defects shows the strength of defects as well as indicates the areas covered by defects. Unfortunately, the gray level map of defects is difficult for analysis both for humans and for the computer. Despite of using the morphological algorithm with reduced noise sensitivity in comparison with a common top-hat transform, one still obtains an image containing many pixels with some shade of gray. This is due to high level of noise in the images of the cores. A further limitation of the described defect detector stems from the fact that the morphological operations use a structuring element for interaction with the image. The result is that the detector is able to detect defects to some degree greater than the structuring element, which in this case is a flat 3×3 square. However, defects which are significantly greater may go unnoticed.

3. Detection of defects by means of the morphological pyramid

In order to detect defects in a wider range of sizes the morphological pyramid is used jointly with the defect detector, as shown in Fig. 2. Such a pyramid is obtained in accordance with the theory developed in [8] and [9]. In general, any pyramid is used for changing the size of the image, or more precisely, for reduction of the resolution. For example, a typical image of size 512×512 pixels is converted into an image of 256×256 pixels, and then into

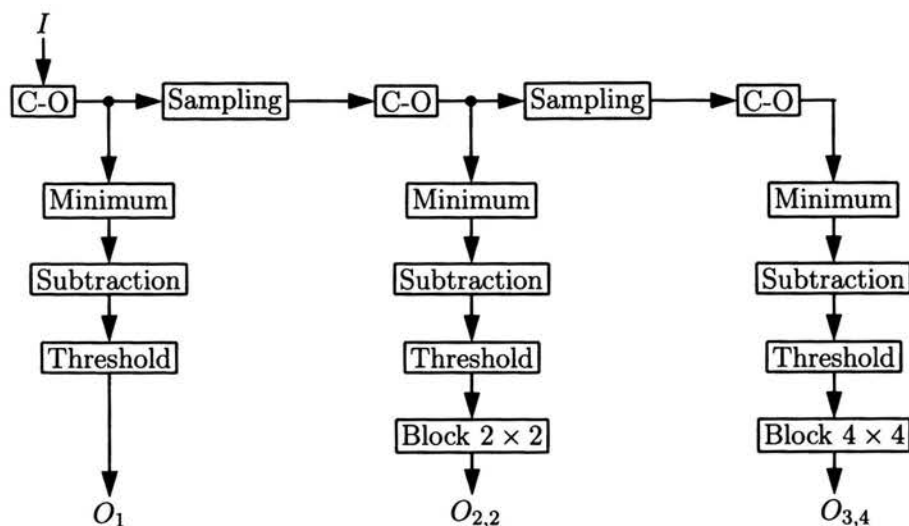


FIGURE 2. Morphological pyramid for detection of positions of defects.

an image of 128×128 pixels, and so on. However, reduction of the size of the image usually involves some loss of information, which means that one could miss some of the defects. The digital morphological sampling theorem in [9] answers the following questions:

1. How a digital image must be morphologically filtered before sampling in order to preserve relevant information after sampling?
2. What is the precision of a morphologically filtered image reconstructed after sampling?
3. What is the relationship between the morphological filtering before sampling *and* the morphological filtering of the sampled image with a sampled structuring element?

Following the above theorem, the morphological pyramid under consideration is generated in such a way that each reduced image is obtained from the previous (larger) one by means of the morphological filtering, in the form of closing followed by opening (the so-called C-O filter), with subsequent sampling of the filtered image. The purpose of the filtering is the removal of noise from the image while keeping the loss of the useful information at a minimum. The sequence of operations for pyramid generation is illustrated by the top horizontal line in Fig. 2. Generation of the map of defects for each level of the pyramid is illustrated by respective vertical lines (columns) in Fig. 2. The thresholding operation near the bottom of each column converts a gray level map of defects into a binary map, in which any pixel having

originally brightness above some chosen threshold is converted into a pixel of brightness 255 (compare Figures 4(b), (c), and (d)), and all the other pixels have brightness 0. In order to convert the low resolution maps of defects to the common (highest) resolution, each pixel in a lower resolution map is repeated appropriate number of times. For example, for the second level of the pyramid, each pixel is repeated in a block 2×2 , as indicated by the operation Block 2×2 in the second column in Fig. 2. The results from the pyramid after binarization and conversion to the highest resolution are O_1 , $O_{2,2}$, $O_{3,4}$, and possibly $O_{4,8}$, if four levels of the pyramid are used.

4. Extraction of the shape of small defects in the image

The first step in the extraction of the shape of small defects is the extraction of all brighter areas in the image [10]. The latter extraction requires a sequence of morphological operations shown in the upper left portion of Fig. 3. For theoretical background of morphological reconstruction the reader is referred to [11]. Thinking about the gray level distribution as a topographical surface over some reference level, one can consider the defects as local hills. Complementing the image under consideration one obtains another image in which the defects represent basins. This is the image called the mask.

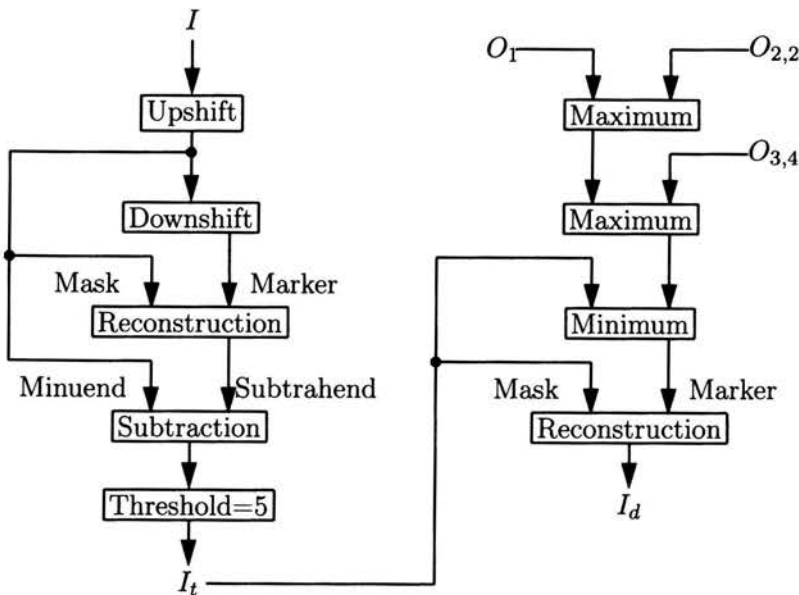


FIGURE 3. Sequence of operations for extraction of the shape of defects.

The reconstruction by dilation [11] simply fills out some of these basins to a certain height. For reconstruction purposes another image, called a marker, must also be used. In the current case, all the brighter areas in the image are taken into account, and for obtaining both the mask and the marker the same input image I is used, moved appropriately on the gray scale, because the marker should lie below the mask. As shown in Fig. 3, the image I is first shifted upwards and then downwards. The chosen value of the upward shift is 35 gray levels. The upshifted image is used as a mask. The chosen downward shift is 25 gray levels. Using two shifts in opposite directions, instead of just one, is of minor importance. However, in this way one obtains a precisely defined difference of the brightness between the mask and the marker at every pixel. Using just the original image I and its upshifted version might reduce the brightness difference at pixels where the defect is very bright and it is impossible to increase brightness above the maximum value of 255. The operation of reconstruction is denoted by $\rho_{\text{mask}}(\text{marker})$, so that the result of the reconstruction can be written as

$$I_r = \rho_{I_{35}}(I_{25}), \quad (4.1)$$

where I_{35} and I_{25} denote the upshifted and downshifted images, respectively. By taking the difference of images $I_{35} - I_r$ pixelwise, one obtains the image of the so called h -maxima [11]. These maxima represent the upper portion of each defect or any other brighter spot in the image. In the case under consideration, the maxima are obtained by cutting off each defect 10 levels below the respective peak. As a result the shape of each defect becomes entirely independent of the local brightness in the image. The h -maxima carry information on defects as well as on any other brighter spots in the image. For the purposes of defect analysis and classification, it is necessary to have the contours of the defects. Hence, the image of h -maxima is binarized by assigning the value zero to all pixels having brightness less than or equal to a predefined threshold

$$I_t = \text{TH}(I_{35} - I_r) \quad (4.2)$$

and assigning 255 to all remaining pixels.

The value of the threshold was experimentally chosen as equal to 5. In general such value should be adjusted to images under consideration. Obviously, the binarized map of h -maxima includes both defects and all other brighter spots. In principle, one wants to keep only the peaks marked by the pyramid and remove all the others. For this, a binary reconstruction by dilation is used. In this reconstruction the image I_t is used as a mask. The marker I_m is formed according to the equation which for four levels of the

pyramid can be written as

$$I_m = \min [\max(O_{1,}, O_{2,2}, O_{3,4}, O_{4,8}), I_t]. \quad (4.3)$$

The max in the above equation denotes the logical summation of all the outputs of the pyramid. The min denotes the intersection of the mask and of the result of summation and is used for making sure that the marker includes exclusively pixels contained in connected components of the mask, that is the marker does not stick out of the mask.

Now the binary reconstruction by dilation is carried out in accordance with the equation

$$I_d = \rho_{I_t}(I_m), \quad (4.4)$$

where I_d is the final map of defects.

There may be very few defects in the image which determine whether the core should be rejected or not. The less critical defects and noise are removed by thresholding the gray level maps of defects at every level of the pyramid. The result of thresholding is a pyramid of binary maps of defects. The thresholds play a decisive role in assigning a given pixel to a defect or to a defect free area. In particular, if the same ferrite core is inspected and the lighting conditions have changed, then the thresholds have to be adjusted accordingly. Manual adjustment of the thresholds is a lengthy procedure requiring a skillful operator. The procedure for automatic change of thresholds is presented in Section 6.

5. Examples of extraction of the shape of small defects

A sequence of operations necessary for the detection of defects and extraction of their shape is illustrated in Fig. 4. In particular, Fig. 4(a) shows the original image of the core. This core has a U-shape, and the figure distinctly shows only the flat surface of one of the legs of the core. The part of the core connecting both legs is dimly visible to the right of the leg, as it is slightly brighter than the black background, on which the core is positioned. Some defects are visible in the upper part of the image, and a small defect is on the left boundary of the core. Figures 4(b)-(d) illustrate the outputs of the individual levels of the pyramid. Figure 4(e) shows the result of the gray level reconstruction I_r , and Fig. 4(f) depicts the binarized h -maxima I_t . In the latter image, one can recognize defects as well as many other brighter spots resulting from unevenness of the surface of the core. Figure 4(g) shows that the logical sum of all the outputs of the pyramid occupies an area slightly larger than the respective defects, which can be recognized by comparing Figs. 4(a) and (f). By taking the minimum of images in Figs. 4(f) and (g),

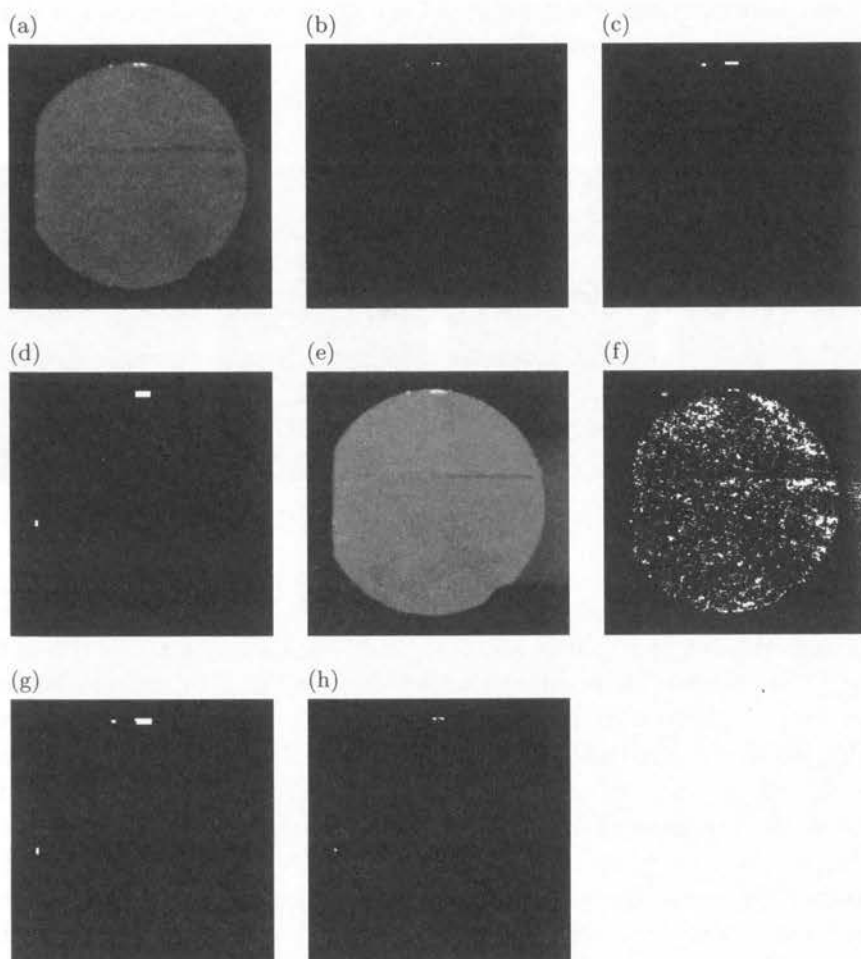


FIGURE 4. Complete example of detection and extraction of small defects. (a) Original image of the ferrite core. (b) Output of the first level of the pyramid O_1 . (c) Output of the second level of the pyramid $O_{2,2}$. (d) Output of the third level of the pyramid $O_{3,4}$. The output of the fourth level of the pyramid $O_{4,8}$ is completely black. (e) Result of the gray level reconstruction I_r . (f) Binarized h -maxima I_t . (g) Logical sum of four levels of the output of the pyramid I_{max} . (h) Map of defects – result of the binary reconstruction I_d .

one obtains the marker I_m , which is not shown here since it would be very similar to Fig. 4(h). The final result of the reconstruction I_d is depicted in Fig. 4(h), where a satisfactory map of defects is visible. In this case defects are relatively small, which is confirmed by the fact that no defects were detected by the fourth level of the pyramid.

Two other examples of extraction of the shape of small defects are shown in Figs. 5(a)-(d). The presented images confirm the viability of the proposed method.

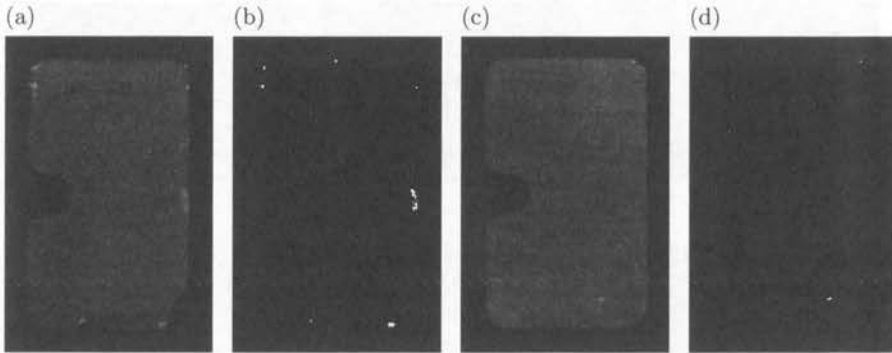


FIGURE 5. (a), (c) Original images. (b), (d) Respective maps of defects.

Another interesting example is shown in Fig. 6. In this case there are two large defects at the bottom of Fig. 6(a), and a small defect at the top of the image. The obtained shapes of the large defects in Fig. 6(b) are very far from satisfactory. This is the result of the fact that these large defects contain very bright, relatively small areas as well as some darker, relatively large areas. The algorithm processes the deepest parts of the defects and extracts the shape of the brightest areas. It is possible to extract the complete shape of the large defects by changing the up- and downshift from the values 35 and 25 mentioned above to 75 and 65, respectively, as illustrated by Fig. 6(c). However, there is a problem that the amount of the required up- and downshift

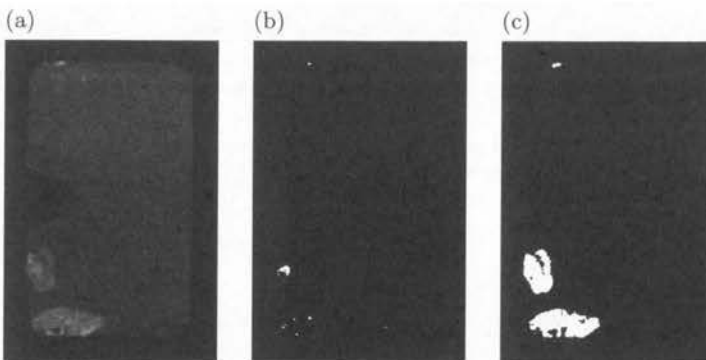


FIGURE 6. (a) Original image. (b) Map of defects. (c) Map of defects obtained for modified up- and downshift.

cannot be adjusted automatically. In such a case, the watershed segmentation is used as described in Sections 7-9. The watershed segmentation, however, still uses the results of extraction of small defects for controlling the process of merging the regions obtained from the watershed segmentation.

6. Genetic algorithm for optimization of the thresholds in the pyramid

The optimization of the thresholds in the pyramid can be made less laborious by using the genetic algorithm [12]. A genetic algorithm imitates biological processes in which stronger individuals have a greater chance of survival [13]. The algorithm described processes a population of 16 individuals, where each individual represents a set of thresholds encoded in a chromosome. The thresholds of the four levels of the pyramid are assumed to be in the range between 0 and $T_{\max} = 63$ and are encoded using the Gray code. Each successive generation is obtained in the following steps:

1. Selection of individuals for the next generation via a scheme called roulette wheel, where the wheel is split into segments proportional to the fitness values of chromosomes in the population.
2. Single crossover mechanism, where the probability of the crossover is $p_c = 0.6$. The crossover point is chosen randomly. The portions of the two chromosomes determined by the crossover point are exchanged to form the new chromosomes.
3. Mutation, where the probability of changing a given bit is equal to a small number $p_m = 0.01$. The mutation introduces a new material into the chromosomes.

A population of chromosomes is modified from one generation to the next based on the fitness value representing the strength of the chromosome for solving the optimization problem. In the case considered, the fitness value is a measure of agreement between the actual configuration of defects for given chromosome and the desired reference configuration obtained independently. The following rules are observed in the implementation of the genetic algorithm:

1. By using the elitist model the chromosome with maximum fitness is kept from one generation to the next and inserted in the place of the worst chromosome. This approach guarantees convergence of the evolution.
2. Random generators with different random seeds are used for every run of the genetic algorithm in order to avoid premature convergence.

3. The thresholds and the values of fitness averaged over all images are kept in memory in order to avoid repetition of calculations for the same chromosomes. The computations are terminated if the maximum allowable number of generations is reached, or if there is no change between successive generations.

The value of the fitness function is calculated based on the following assumptions. The measure of defectiveness is disregarded, and the only available information is whether a pixel belongs to a defect or not. The binary maps of defects for all levels of the pyramid for given image are recalculated to the highest resolution. The union of these maps for all levels for given input image and given chromosome is found. The resulting image is called the actual binary map A_{act} of defects. The respective reference binary map of defects for the same image is denoted by A_{ref} . It was found experimentally that a convenient form of the fitness function f is

$$f = 10000 \frac{\#(A_{ref} \cap A_{act})}{\#(A_{ref} \cup A_{act})}. \quad (6.1)$$

The numerator of Eq. (6.1) indicates how many pixels are in the intersection of the reference map and the actual map, whereas the denominator shows how many pixels are in the union of the same maps. The coefficient of 10000 was found experimentally. The overall fitness of a given chromosome for all the images is equal to the average of the values obtained for individual images. In accordance with [13], the algorithm uses the rescaled fitness value f_s rather than f in calculations:

$$f_s = af + b. \quad (6.2)$$

The parameters a and b are chosen in such a way that the average values of f_s and f are the same for a given generation, and the scaled maximum fitness is equal to twice the average fitness for the chromosome population. Should the minimum become negative, then it is set equal to zero and a and b are recalculated so that the average values of f_s and f are equal.

The principle of operation of the algorithm for generating the optimal thresholds is as follows. The initial generation of chromosomes is generated with random values. For each chromosome, the set of thresholds is obtained by decoding the chromosome. Subsequently, these thresholds are used in the morphological pyramid for generating the actual lists of defects for each chromosome and each training image. After evaluating the fitness for all of the chromosomes, the algorithm decides whether to continue or to terminate the computations. If the decision is to continue, then the current generation of chromosomes is used as an input to the genetic algorithm, which in response

delivers the next generation of chromosomes, and subsequently the loop of computations is repeated.

Experimental results from the genetic algorithm are illustrated in Figs. 7 and 8. For these experiments, a set of eight training images was chosen as an input to the genetic algorithm. Figures 7(a)-(d) show four levels of the pyramids for an example of a training image. In Fig. 7(e) the reference binary map of defects for this example is depicted. Such maps were obtained by means of the software for defect classification [14]. Figure 7(f) shows the actual map obtained by the system described. This map corresponds to the

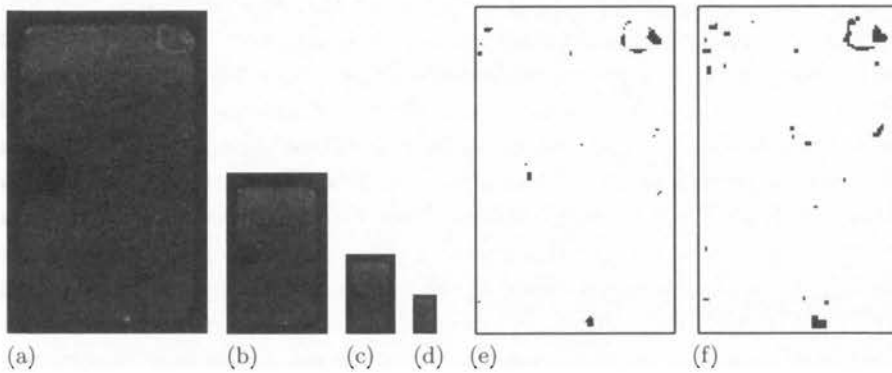


FIGURE 7. Optimization of the thresholds in the pyramid by means of the genetic algorithm. (a)-(d) Pyramid for one out of eight training images, (e) Reference binary map of defects for the respective image, (f) Actual binary map of defects obtained by means of the genetic algorithm.

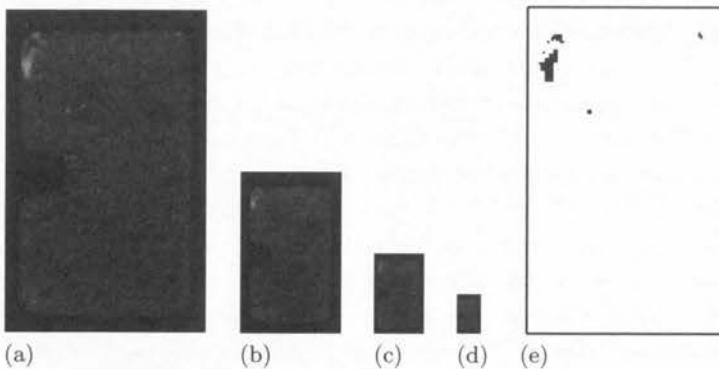


FIGURE 8. Defect detection for a test image. (a)-(d) Pyramid for a test image. (e) Binary map of defects for the test image, obtained with the thresholds optimized by the genetic algorithm.

optimal thresholds 23, 9, 10, 19, found after 320 generations, respectively, for the highest through lowest resolution. Figures 8(a)-(d) show four levels of the pyramid for a chosen test image. Figure 8(e) depicts the binary maps of defects obtained for this image when using the optimal thresholds for the training set.

7. Using the watershed segmentation algorithm for extraction of large defects

Watershed segmentation is discussed here shortly since there are many publications on this subject [11], [15]-[19]. In this approach, the gray level image is considered as a topographical relief, and the brightness of each pixel corresponds to a physical elevation. The rain falling on such a relief accumulates in the depressions of the terrain. Each depression defines its own catchment basin, which corresponds to a certain region in the image. The watershed algorithm is usually implemented in a different way, by simulation of the flooding of the terrain starting from the so called regional minima. It is assumed that the regional minima of the relief are pierced, and the relief is slowly immersed into the "lake". Water comes in and rises up in various catchment basins as the relief gets deeper and deeper into the lake. As soon as two catchment basins tend to merge, a dam is built. The lines representing the dams are called watershed lines. The watershed procedure results in a partitioning of the image into catchment basins, or regions.

In [11] the watershed segmentation is obtained by finding the Skeleton by Influence Zones (SKIZ). This is basically a geometric approach, which analyzes the image globally. In the described calculations a local analysis was used, in which only a neighborhood of a current pixel is considered [20]. In principle, both methods are appropriate for identification of large defects. The main advantage of the used method lies in its simplicity.

More critical than the implementation of the watershed algorithm itself are the problems specific to the images of defects. In many cases described in the literature, the watershed is used for finding contours of relatively large objects. Defects, on the contrary, may be large or small and may possess a complicated, unpredictable structure, evidenced not only by their contour but also by varying depth. The watershed segmentation typically results in a partitioning of the image into many small regions that do not have a clear intuitive meaning. However, in the case of defects the ideal output from the watershed segmentation would consist of just two regions: one representing a defect, and the other covering a defect free area. As this is improbable, one would like at least to have a small number of regions covering the defect and the defect free area. This simplified partition description does not suggest,

however, that there may be any region covering partly the defect and partly the defect free area.

In order to avoid the oversegmentation, the original image of the core is first filtered by means of the C-O filter. It was found experimentally that using a 3×3 structuring element simplifies the image and does not introduce false boundaries in the watershed segmentation. Furthermore, the watershed segmentation is carried out on the gradient image rather than on the original image itself. As a result, the regions are determined by the edges of the core and defects. A simple morphological gradient definition is that in which the gradient is proportional to the difference of dilation and erosion of a given image. However, this gradient gives poor results in the case when the edge of the object should be modelled by the ramp function rather than by the step function [18]. In addition, this gradient is also poor in separation of two edges which are close one to the other. The images of defects abound in edges for which the most appropriate model is the ramp function, and the edges can come close together. Experiments showed that using the above, conventional gradient (the so called mono-scaled gradient) results in regions that do not fit well into the shape of defects. In such a case, significantly better results are obtained with a multi-scale morphological gradient. In practice, the two-scale gradient G_r defined by the equation [18]

$$G_r = 1/2 \{[(I \oplus B_1) - (I \ominus B_1)] + [(I \oplus B_2) - (I \ominus B_2)] \ominus B_1\} \quad (7.1)$$

turned out to be sufficient. B_1 and B_2 in Eq. (7.1) are structuring elements of size 3×3 and 5×5 , respectively. The symbol \oplus stands for dilation, and \ominus for erosion. The two-scale morphological gradient uses the sum of two mono-scale gradients obtained with different structuring elements, with the stipulation that the result obtained with the larger structuring element is additionally eroded using the smaller structuring element.

In order to restrict the oversegmentation even further, the obtained gradient image is thresholded by changing to zero all the pixels with brightness up to 10. Although [18] suggests the reconstruction by erosion for the removal of small local minima, experiments with images of ferrite cores showed that such a reconstruction gives results which are no better than those obtained with the thresholding of the gradient. The consistency of the boundaries of the regions obtained by the watershed segmentation with recognizable edges of defects can be observed in all images presented in Section 9.

8. Classifier of watershed regions

The results obtained from the watershed segmentation are only partly satisfactory. A human can recognize that some regions belong to the defect,

and some to the defect free area. However, the watershed algorithm cannot decide which regions should be included into defects, and which not. It might seem that by using some threshold one could classify brighter regions to the defect, and darker regions to the defect free area. This turned out impossible, however, because the brightness difference between the defect and the surroundings may be quite low, and besides the threshold should be adjusted for each image separately. Any misclassification of a region may result in a significant error since regions tend to occupy relatively large areas.

The region classifier generates the final map of defects using the results of the watershed segmentation and of the merging of the regions with similar brightness. In addition, the region classifier also utilizes the information from the map of small defects, which may be considered as a some kind of a seed for the generation of the mask of a defect.

The detailed operation of the region classifier is as follows. First of all, the regions are sorted based on the average value of their brightness g_i , and all the regions with $g_i \leq 50$ are removed since such low g_i indicates that one has to do with the background rather than with a properly lit surface. Then the average brightness G of all included regions is calculated. Subsequently for each pixel in the map of small defects the region is found to which this pixel belongs. In this way a list l is created of all regions having at least one pixel belonging to a defect. This list is then reduced to a short list l_s with all multiple entries removed. Subsequently the list l_s is scanned and all the regions satisfying the condition $g_i > G$ have all their pixels marked white for indicating defects. The condition $g_i > G$ is a safeguard against the situation when some accidental pixel or two belonging to the map of small defects mark a region with low g_i as belonging to a defect, which is unreasonable. The regions classified so far as belonging to defects represent the main part of each defect; however, sometimes further completion of the mask of a defect is necessary. This time all the regions for which $g_i > 50$ are processed. If a current region i is not on the short list l_s , but has a neighbor on this list, and besides if the $g_i > G + 15$, then the current region i is considered as a part of the defect and all its pixels are marked white. The viability of the described region classifier was confirmed by many experiments, as illustrated in the next section.

9. Experimental results of extraction of the shape of large defects

A complete example of the identification of a large defect is shown in Fig. 9, for a window taken from the lower left part of Fig. 6(a) and shown again in Fig. 9(a).

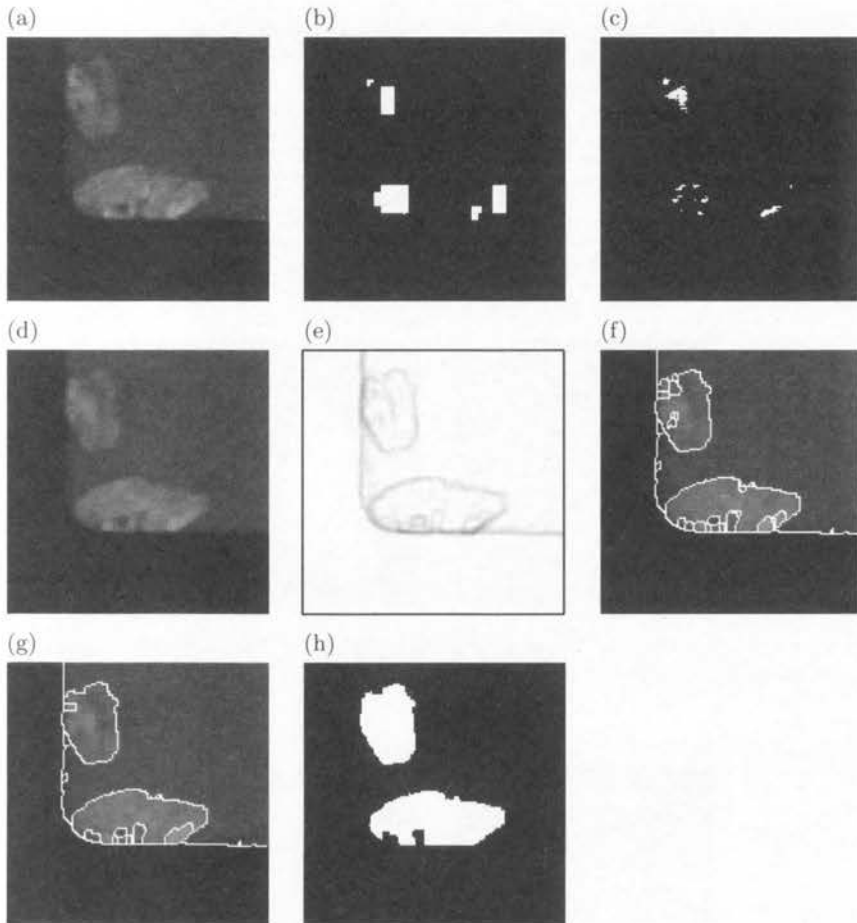


FIGURE 9. (a) Window of size 150×150 taken from the image in Fig. 6(a). (b) Map of defects obtained by the logical summation of outputs of four levels of the pyramid for image (a). (c) Result of extraction using the method for small defects. (d) Image filtered by means of the C-O. (e) Complement of the two-scale morphological gradient after thresholding. (f) Result of the watershed segmentation. (g) Result of region merging. (h) Final map of defects.

Figure 9(b) depicts the result obtained from the pyramid. The positions of defects are shown correctly, but the shape is not. The map of small defects in Fig. 9(c) presents a window taken from Fig. 6(b). One can observe that this map shows small defects, which in this case just happen to be the brightest parts of large defects. The image in Fig. 9(d) depicts the result of the C-O filtering of the image in Fig. 9(a). The complement of the thresholded gradient of the image in Fig. 9(d) is shown in Fig. 9(e). The number of regions obtained

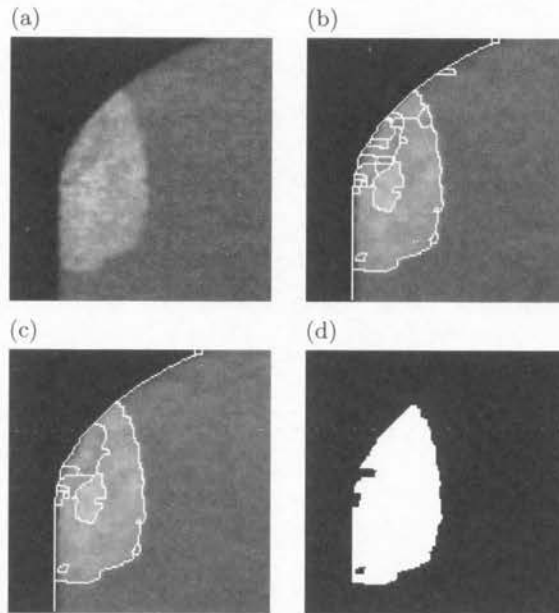


FIGURE 10. (a) Original image of the ferrite core. (b) Result of watershed segmentation. (c) Result of region merging. (d) Final map of defects.

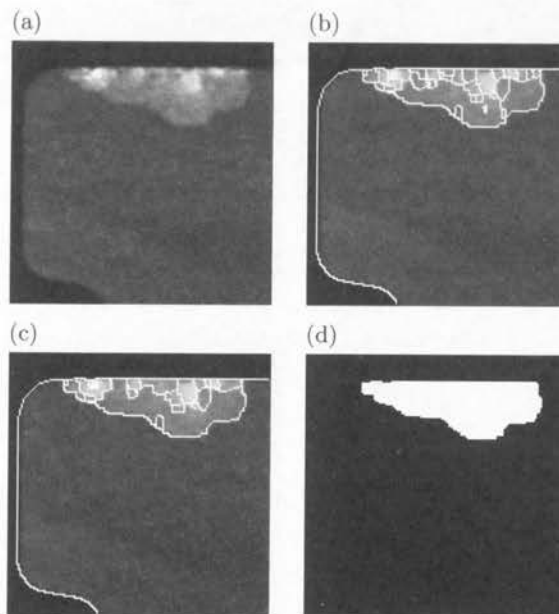


FIGURE 11. (a) Original image of the ferrite core. (b) Result of watershed segmentation. (c) Result of region merging. (d) Final map of defects.

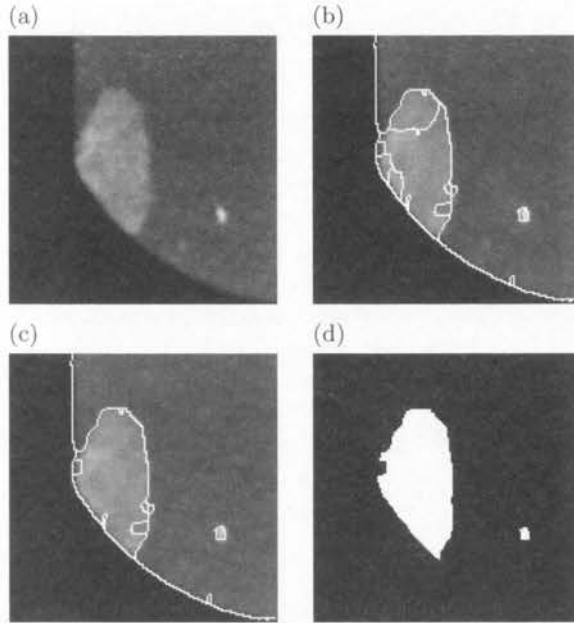


FIGURE 12. (a) Original image of the ferrite core. (b) Result of watershed segmentation. (c) Result of region merging. (d) Final map of defects.

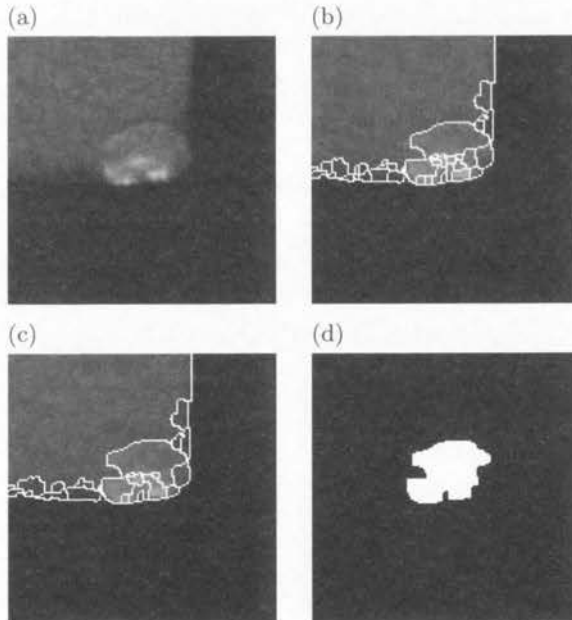


FIGURE 13. (a) Original image of the ferrite core. (b) Result of watershed segmentation. (c) Result of region merging. (d) Final map of defects.

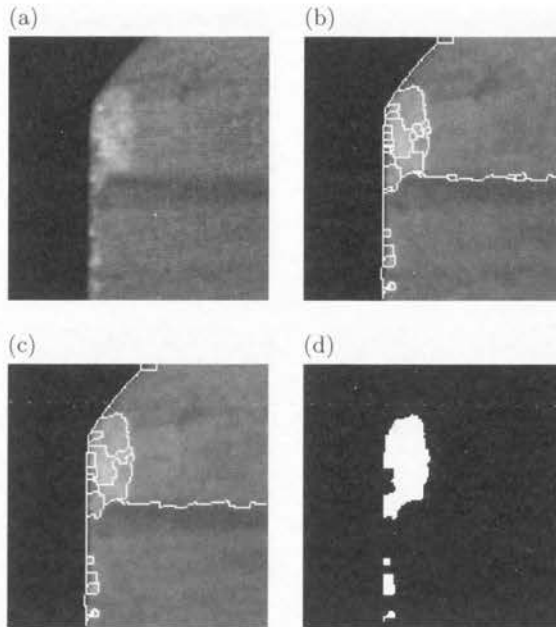


FIGURE 14. (a) Original image of the ferrite core. (b) Result of watershed segmentation. (c) Result of region merging. (d) Final map of defects.

by the watershed segmentation is 28 (Fig. 9(f)), and in this particular case almost all regions belong to two defects, whereas the defect free area consists in principle of a single large region. The number of regions after merging is 16 (Fig. 9(g)). The final map of defects is shown in Fig. 9(h). The vision system described was used for testing a larger number of diversified images (Figs. 10–14), and in all cases the masks of defects had a correct shape.

Apart from detection and extraction of large defects, it may be necessary to carry out their classification as well. Then the map of defects obtained from the vision system is input into the defect classifier.

10. Extraction of cracks

The cracks are just one form of defects in ferrites. Sometimes one form of the defect can go over into another, for example a crack can widen and become a chip. This situation suggests that crack extraction might be a particular case of (any) defect extraction.

There exist some papers dealing directly with extraction of cracks [21, 22]. The PhD dissertation [22] analyzes images containing lines, both straight and curved. It develops a model in which an image is represented by an unknown

number of Bézier curves. The parameters of the model are obtained by reversible jump Markov chain Monte Carlo technique. The main application considered in [21] and [22] is the classification of the craquelures of old oil paintings. Ferrite cores usually do not exhibit such nets of cracks as are typical for old paintings. The industrial cracks are more localized and hidden so the discussed method does not seem appropriate.

Attempts have been made by the author of the present paper to develop an adaptive genetic algorithm for extraction of cracks based on [23] or an evolutionary system based on [24]. In [23] the genetic algorithm is used for finding the optimal morphological filter for removing artificially introduced noise into texture images from Brodatz album. The genetic algorithm determines both the sequence of operations and the optimal structuring element. In [24] the evolutionary system is used for optimization of the sequence of operations aiming at recognition of letters. The system was tested mainly on binary images, with possible extension to gray level images. Experience of the author was only partly satisfactory. Although it is possible to employ these innovative techniques, they are complicated and give results that are by no means better than the results obtained by a simpler method described below. In particular, it turned out impossible to increase the discriminative power of the crack detector by taking samples of the texture corresponding to cracks and crack free areas and using them for generation of structuring functions which would discriminate between cracks and stripes remaining sometimes on the surface of the cores after the manufacturing process.

The morphological crack detector described below is a modification of the defect detector presented in Section 2. The difference is that the current detector is an anisotropic one, hence more appropriate for crack detection since cracks usually have a form of a long thin and (approximately) straight line segment or consist of some number of such segments.

Additionally, the anisotropy of the detector allows one to better cope with the pattern of parallel stripes which come from the grinding process [25]. An example of the ferrite core with stripes from grinding is shown in Fig. 15(a). The stripes have the appearance of more or less parallel darker and brighter lines. There is a single bright crack visible in Fig. 15(a) in the upper half of the core. The physical length of the core is 50 mm, and the image shows almost the entire core. The size of the image is 128×512 pixels.

In order to carry out the described anisotropic morphological operations, the structuring element should be either perpendicular or parallel to the stripes from grinding. The rotation of the ferrite core itself on the production line is out of the question since this would be a costly manufacturing operation requiring additional equipment; it would also take a long time. The rotation of small structuring elements, for example of size 1×5 , by an

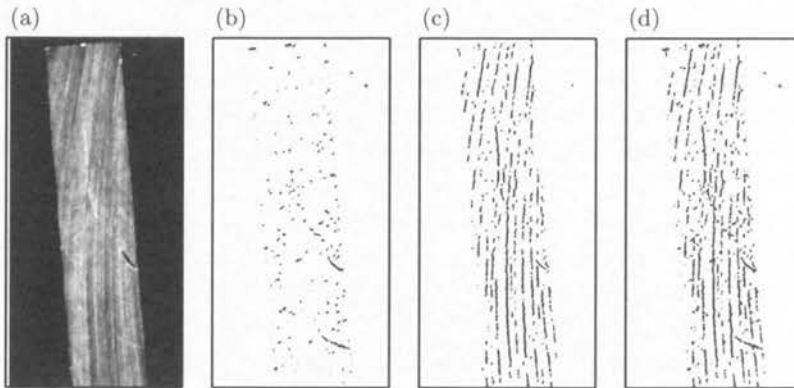


FIGURE 15. Extraction of cracks. (a) Original image. (b) Binary map of horizontal cracks. (c) Binary map of vertical cracks. (d) Final map of cracks. All maps are complemented in this figure.

arbitrary angle, can only be implemented in a very rough manner since the original pixel in general would not fall after rotation exactly into another pixel and some approximation would be necessary. As a result, it turned out more practical to rotate the image of the core. In order to rotate the image, one has first to establish the dominant direction in the image and then rotate the image appropriately. The problem of detection of the dominant direction is known from literature [26] and will not be discussed here. Similarly, the problem of high-accuracy rotation of images using bilinear interpolation of bicubic splines is adequately described in [27]. In the experiments described below, the images of the cores were rotated by means of the commercial program, such as the Photoshop. The accuracy of the vertical (or horizontal) alignment of the stripes in the image is not critical. This is because the used structuring elements are of size, say, 1×5 , with 1 denoting the width, and 5 denoting the height of the element. The stripes usually are two or more pixels wide, which means that the vertical stripe can accommodate such element even if the stripe deviates 10 to 20° from the vertical line. In fact Fig. 15(a) shows the image after rotation.

Detection of horizontal cracks brighter than the surroundings is based on an equation which is a modification of Eq. (2.1)

$$T_h = I - \min[(I \bullet S_h) \circ S_h, I], \quad (10.1)$$

where I denotes the input image, T_h is the gray level map of horizontal cracks, and S_h is a structuring element for detection of horizontal cracks. Detection of cracks darker than the surroundings is possible using an equation dual

to Eq. (10.1)

$$T_h = \max[(I \circ S_h) \bullet S_h, I] - I, \quad (10.2)$$

in which the opening and closing are exchanged, the minimum is replaced by maximum, and the roles of minuend and subtrahend are also exchanged. Due to similarities of analysis, in the following only the cracks brighter than the surroundings are considered.

For detection of horizontal, elongated cracks the *vertical* structuring element of size 1×5 is more appropriate. It was found experimentally that the length of the structuring element is not critical, and for the given size of the cores and of the images the elements of length 3 or 7 might be used as well.

Equation for detecting the vertical cracks is almost the same as Eq. (10.1)

$$T_v = I - \min [(I \bullet S_v) \circ S_v, I]. \quad (10.3)$$

The only difference is that for obtaining the gray level map of vertical cracks the structuring element S_v is used, which is in fact a *horizontal* element of size 5×1 . Summarizing, in order to detect a crack in a given direction, one has to use the structuring element which straddles across the crack.

The images T_h and T_v are gray level maps. After thresholding and complementing, one obtains the binary maps

$$T_{h5} = \text{TH}_1(\bar{T}_h), \quad T_{v5} = \text{TH}_1(\bar{T}_v), \quad (10.4)$$

in which all pixels having measure of defectiveness below certain threshold have brightness 255 (are white), and all other pixels have brightness 0. This means that the cracks are conveniently painted in black (or gray) on white background. The threshold value of 5 was chosen experimentally for Eqs. (10.4). The main idea is to have a low threshold so that everything that might be suspected of being a crack would be included in the map.

It can be seen in Fig. 15(a) that it is quite hard to distinguish between cracks and brighter stripes from grinding. Thresholding the gray level maps of cracks gives binary maps which contain masks of both cracks and bright stripes from grinding. In order to improve the binary maps of cracks the following approach is used.

The gray level maps are thresholded again, this time, however, with a higher threshold equal to 15, so that Eqs. (10.4) are replaced by

$$T_{h15} = \text{TH}_2(\bar{T}_h), \quad T_{v15} = \text{TH}_2(\bar{T}_v). \quad (10.5)$$

The idea behind this operation is that cracks are slightly brighter than bright stripes from grinding. As a result one obtains at least some parts of the cracks, and at the same time one gets rid of some stripes from grinding.

The extraction of the shape of cracks is carried out by means of the binary reconstruction by dilation. Strictly speaking, two separate reconstructions are now carried out: for horizontal and vertical cracks, according to the equations

$$I_h = \rho_{T_{h5}}(T_{h15}), \quad I_v = \rho_{T_{v5}}(T_{v15}). \quad (10.6)$$

The results of reconstruction of vertical and horizontal cracks are depicted in Figs. 15(b) and (c). The map in Fig. 15(b) is in principle satisfactory. The short pseudo-masks representing noise rather than real cracks can be filtered out quite easily. On the contrary, the map in Fig. 15(c) contains masks of cracks together with masks of bright stripes from grinding. By taking the minimum of the complemented maps $\overline{I_h}$ and $\overline{I_v}$, one obtains the complement

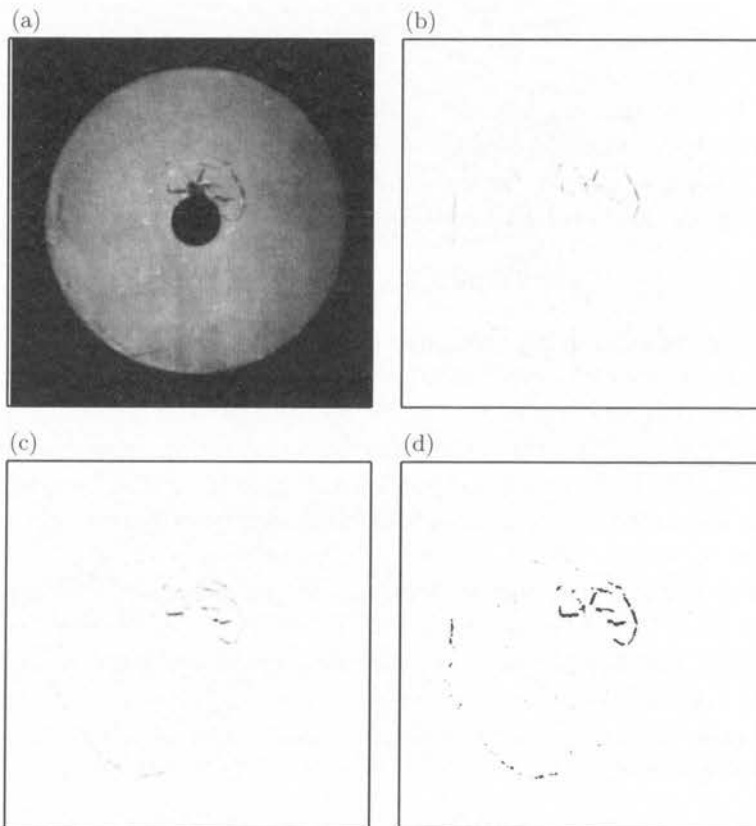


FIGURE 16. Detection of cracks. (a) Original image. (b) Gray level map of vertical cracks. (c) Gray level map of horizontal cracks. (d) Final binary map of cracks. Extraction by reconstruction is not shown in this figure.

of the final map \overline{I}_m of cracks

$$\overline{I}_m = \max(\overline{I}_h, \overline{I}_v). \quad (10.7)$$

The map \overline{I}_m is shown in Fig. 15(d). Obviously the obtained mask cannot be used in the present form, and it is necessary to use the classification procedure for removing the masks of bright stripes [25]; unfortunately, even the classification procedure is not able to completely remove the masks of vertical stripes.

An entirely successful example of extraction of the mask of cracks is given in Fig. 16. Figure 16(a) shows the original image, and Figs. 16(b) and (c) show the gray level maps of vertical and horizontal cracks, respectively. The size of the structuring elements is 3×1 and 1×3 . In order to improve the visibility the actual results from Eqs. (10.1) and (10.3) are multiplied by 3 and complemented. Subsequently, a resulting gray level map of cracks is obtained by taking the minimum of images in Figs. 16(b) and (c) pixelwise, and finally the result is thresholded with the threshold 30, giving the binary map shown in Fig. 16(d). The slanted parts of the cracks are detected partly by the vertical and horizontal structuring elements.

11. Conclusions

Examples presented confirm that the described vision system correctly identifies defects of ferrite cores. This vision system is, to the best of the author's knowledge, the first of its kind. Up to now human operators have been used for the tedious work of the core evaluation. Comparison of the results obtained from the vision system with opinions of the experts show that they agree most of the time, although it did happen several times that the expert was not quite sure in his opinion. The execution time of defect detection and extraction operations is on the order of 1-2 seconds so that they can be carried out in real-time. The execution time of the watershed segmentation can be reduced to similar values with up-to-date software and a Pentium IV computer. Taking decision regarding the acceptance or rejection of a core requires calculation of certain statistics for the obtained masks of defects, for example the area of the defect. These calculations can also be done in real-time. However, up to now the overall experimental vision system has not been optimized for speed. The described system can be used, with some adjustments, for many other industrial products, for example ceramic materials.

References

1. M. MARI et al., The CRASH project: defect detection and classification in ferrite cores, *Image Analysis and Processing*, (A. Del Bimbo, Ed.), Vol.II, pp.781-787, Springer Verlag, Berlin 1997.
2. M. NIENIEWSKI and R. SERNEELS, Detection and extraction of the shape of defects on the surface of ferrite cores, *Proceedings of the 2nd IEEE Benelux Signal Processing Symposium*, Hilvarenbeek 2000.
3. F. HUET and J. MATIOLI, A textural analysis by mathematical morphology, *Mathematical Morphology and Its Applications to Image and Signal Processing*, (P. Maragos et al., Eds.), pp.297-304, Kluwer Academic Publishers, Boston 1996.
4. D. G. DAUT and D. ZHAO, A flaw detection method based on morphological image processing, *IEEE Transactions on Circuits and Systems for Video Technology*, Vol.3, No.6, pp.389-398, 1993.
5. P. SALEMBIER, Comparison of some morphological algorithms based on contrast enhancement – application to automatic defect detection, *Signal Processing V (EU-SIPCO V)*, (L. Torres et al., Eds.), pp.833-836, Elsevier, Amsterdam 1990.
6. P. SALEMBIER, Multiresolution decomposition and adaptive filtering with rank order based filters – application to surface defect detection, *Proceeding of the International Conference on Acoustics, Speech, and Signal Processing*, pp.2389-2392, Toronto 1991.
7. L. CHMIELEWSKI, M. SKŁODOWSKI, and W. CUDNY, *Classification of defects on the surface of black ceramics*, this volume: pp.203-230.
8. M. NIENIEWSKI, Morphological method for detecting defects on the surface of ferrite cores, *Proc. of the 10th Scandinavian Conference on Image Processing*, Vol.I, pp.323-330, Lappeenranta 1997.
9. M. R. HARALICK et al., The digital morphological sampling theorem, *IEEE Transactions on Acoustics, Sound, and Signal Processing*, Vol.37, No.12, pp.2067-2090, 1989.
10. M. NIENIEWSKI and R. SERNEELS, Extraction of the shape of small defects on the surface of ferrite cores, *Machine Graphics and Vision*, Vol.9, No. 1-2, pp.453-462, 2000.
11. P. SOILLE, *Morphological Image Analysis*, Springer Verlag, Berlin 1999.
12. T. NGUYEN and M. NIENIEWSKI, Optimization of the morphological pyramid for detecting defects on the surface of ferrite cores, *Proceeding of the 10th Annual Conference Industrial Electronics Society*, Vol.3/4, pp.1273-1278, Aachen 1998.
13. D. E. GOLDBERG, *Genetic Algorithms in Search, Optimization, and Machine Learning*, Addison-Wesley, Reading, MA, 1989.
14. A. JÓZWIK et al., A 1-NN preclassifier for fuzzy k-NN rule, *Proceedings of the International Conference on Pattern Recognition*, Vol.IV, track D, pp.234-238, Vienna 1996.
15. S. BEUCHER, Watershed, hierarchical segmentation and waterfall algorithm, *Mathematical Morphology and Its Application to Image Processing*, (J. Serra and P. Soille, Eds.), pp.69-76, Kluwer Academic Publishers, Dordrecht 1994.

16. J. M. GAUCH Image segmentation and analysis via multiscale gradient watershed hierarchies, *IEEE Transactions on Image Processing*, Vol.8, No.1, pp.69-79, 1999.
17. K. HARIS et al., Hybrid image segmentation using watersheds and fast region merging, *IEEE Transactions on Image Processing*, Vol.7, No.12, pp.1684-1699, 1998.
18. D. WANG, A multiscale gradient algorithm for image segmentation using watersheds, *Pattern Recognition*, Vol.30, No.12, pp.2043-2052, 1997.
19. M. NIENIEWSKI and R. SERNEELS, Vision system identification of large defects on the surface of ferrite cores, *Proceedings of the 11th Portuguese Conference on Pattern Recognition*, pp.345-352, Porto 2000.
20. R. SERNEELS, M. NIENIEWSKI, and E. E. KERRE, Segmentation of images using a simplified watershed algorithm, *Intelligent Techniques and Soft Computing in Nuclear Science, Proc. of the 4th International Conference, Bruges 2000*, (Da Ruan et al., Eds.), pp.231-238, World Scientific, Singapore 2000.
21. D. PALMER, Splitting images, *Cambridge Alumni Magazine*, pp.21-22, 1997.
22. A. J. VARLEY, *Statistical Image Analysis Method for Line Detection*, PhD dissertation, University of Cambridge, UK, 1997.
23. W. LI, V. HAESE-COAT, AND J. RONSIN, Using adaptive genetic algorithms in the design of morphological filters in textural image processing, *Nonlinear Image Processing, SPIE*, Vol.2662, pp.24-35, 1997.
24. M. A. ZMUDA, L. A. TAMBOURINO, and M. M. RIZKI, An evolutionary learning system for synthesizing complex morphological filters, *IEEE Transactions on Systems, Man, and Cybernetics*, Vol.26, No.4, pp.645-653, 1996.
25. M. NIENIEWSKI et al., Morphological detection and feature-based classification of cracked regions in ferrites, *Machine Graphics and Vision*, Vol.8, No.4, pp.699-712, 1999.
26. G. Z. YANG et al., Structure adaptive anisotropic filtering for magnetic resonance image enhancement, *Proceedings of the 6th International Conference on Computer Analysis of Images and Patterns (CAIP)*, pp.384-391, Springer Verlag, Berlin 1995.
27. P. E. DANIELSSON and M. HAMMERIN, High accuracy rotation of images, *Computer Vision, Graphics, and Image Processing*, Vol.54, No.4, pp.340-344, 1992.

